Effect of sample preparation techniques upon single cell chemical imaging : a practical comparison between synchrotron radiation based X-ray fluorescence (SR-XRF) and Nanoscopic Secondary Ion Mass Spectrometry (nano-SIMS)

Effect of Sample Preparation Techniques upon Single Cell Chemical Imaging: A Practical Comparison between Synchrotron Radiation based X-ray Fluorescence (SR-XRF) and Nanoscopic Secondary Ion Mass Spectrometry (nano-SIMS)

Authors & Affiliations

[1*]Björn De Samber, [2,3]Riet De Rycke, [2,3]Michiel De Bruyne, [4]Michiel Kienhuis, [5,6]Sylvain Bohic, [6]Peter Cloetens, [7]Constantin Urban, [4]Lubos Polerecky, [1]Laszlo Vincze

[1]Department of Chemistry, Ghent University, Belgium

[2]Department for Biomedical Molecular Biology, Ghent University, Belgium and VIB Center for Inflammation Research, Ghent, Belgium

[3]Ghent University Expertise Centre for Transmission Electron Microscopy and VIB BioImaging Core, Ghent, Belgium

[4]Department of Earth Sciences – Geochemistry, Faculty of Geosciences, Utrecht University, The Netherlands

[5]Inserm, UA07, Synchrotron Research for Biomedicine, Grenoble, France

[6]European Synchrotron Radiation Facility, Grenoble, France

[7]Department of Clinical Microbiology, Umeå University, Umeå, Sweden

*Corresponding author & full address:
Björn De Samber
X-ray Imaging and Microspectroscopy group (XMI)
Department of Chemistry
Krijgslaan 281 –S12
B-9000 Gent
BELGIUM

Keywords

Synchrotron radiation, X-ray fluorescence, XRF; nano-SIMS, cell imaging, sample preparation

Abstract

Analytical capabilities of Nanoscopic Secondary Ion Mass Spectrometry (nano-SIMS) and Synchrotron Radiation based X-ray Fluorescence (SR nano-XRF) techniques were compared for a specific single cell imaging case study: high pressure frozen (HPF) and cryo-substituted polymorphonuclear neutrophils (PMNs). Nano-SIMS enabled nanoscale mapping of isotopes of C, N, O, P and S, while SR based nano-XRF enabled trace level imaging of metals like Ca, Mn, Fe, Ni, Cu and Zn at a resolution of approx. 50 nm. The obtained elemental distributions were compared with those of whole, cryofrozen PMNs measured at the newly developed ID16A nano-imaging beamline at the European Synchrotron Radiation Facility (ESRF) in Grenoble, France. Similarities were observed for elements more tightly bound to the cell structure such as phosphorus and sulphur, while differences for mobile ions such as chlorine and potassium were more pronounced. Due to the observed elemental redistribution of mobile ions such as potassium and chlorine, elemental analysis of high pressure frozen (HPF), cryo-substituted samples should therefore be interpreted critically. Although decreasing analytical sensitivity occurs due to the presence of ice, analysis of cryofrozen cells - close to their native state - remains the reference method *par excellence*. In general, we found nanoscale secondary ion mass spectrometry (nano-SIMS) and synchrotron radiation based nanoscopic X-ray fluorescence (SR nano-XRF) to be two supplementary alternatives, each with their own pros and cons, to investigate single cells at the nanoscale.

Introduction

Among the label-free, elemental imaging techniques (i.e. no chemical staining, no fluorescent probes), capable of subcellular resolution, two techniques especially stand out: synchrotron radiation-based nanoscopic X-ray fluorescence (SR nano-XRF) and nanoscale secondary ion mass spectrometry (nano-SIMS). Both nano-SIMS [1-6] and SR nano-XRF [7-14] have already been used extensively for nano-imaging of cells and tissues. Although both techniques provide nanochemical imaging, they differ in a number of aspects. While nano-SIMS bombards the sample surface with a focused ion beam, resulting in sputtered secondary ions, nano-XRF ejects inner core-shell electrons, resulting in secondary fluorescent photons. The main analytical difference is that nano-SIMS can distinguish between different isotopes of the same element (e.g., ^{56}Fe and ^{57}Fe), whereas SR nano-XRF imaging only relates to the atomic number. Table 1 provides an overview of the most important properties and differences of both techniques with emphasis on cell imaging. In principle, both techniques are available for the general scientific community upon request, taking into account their availability.

Both nano-SIMS and SR based nano-XRF significantly differ in terms of required sample preparation. For nano-SIMS, samples need to be made compatible with a high vacuum environment and also need to be made as flat as possible, ideally few nanometers. Biological samples for nano-SIMS analysis are therefore first fixed chemically (or cryogenically). Note that for cryogenic fixation, high pressure freezing (HPF) is known to retain the cellular ultrastructure best [15-18]. Although the required following cryo-substitution step can slow down the diffusion of unbound elements such as potassium, the complete retention of other elemental distributions with this method is still debated. Samples are then embedded in a resin (e.g. Spurr, LR white), cut in (sub)micrometer thin-sections, deposited onto pure conducting silicon chips (or polycarbonate filter paper) and additionally gold-coated when necessary to avoid charging. Although not yet commercially available, work is ongoing to develop analysis of cryogenically frozen specimens with nano-SIMS (5). With respect to sample preparation for SR-XRF scanning of biological samples, majority of samples is still analyzed under ambient temperature and atmosphere. In this case, the stability of the sample throughout the X-ray scanning procedure is assured by chemical fixation followed by embedding, or cryofixation followed by necessary freeze-drying. As sample support for cells, silicon nitride (Si_3N_4) membranes are often the preferred choice, resulting in minimal X-ray scatter and low XRF background.

Since recently, a few hard X-ray nanoprobes worldwide are even offering analysis under cryogenic conditions where cryofrozen (vitrified) samples can be directly inserted in the instrument without the need of chemical fixation and embedding or freeze-drying [9, 19]. Preceding sample preparation generally involves a brief wash of the adhered cells on silicon nitride wafers with an appropriate buffer solution to remove trace metal rich medium, followed by gentle blotting of the sample to remove the excess layer of water covering the cells, causing detrimental absorption of fluorescent X-rays when frozen. Then, intra- and extracellular content are trapped via cryogenic fixation using plunge (snap) freezing, which is compatible with larger samples. Just like in the case of high pressure freezing (HPF), plunge freezing avoids damage of the cell ultrastructure by ice crystal formation, which takes place during slow freezing. Elemental distributions are kept intact in the cellular hydrated environment of the vitrified cells since no fixation or resin infiltration has caused diffusion of metal ions. Vitrified samples are then shipped to the synchrotron site in a dry-shipper and finally transferred to the beamline cryogenic sample environment, maintaining the samples at cryogenic temperature uninterruptedly and ensuring the cryogenic workflow.

PROPERTY	NANO-SIMS	SR NANO-XRF
Probe	focused ion beam (Cs^+ or O^-)	focused high-energy photon beam
Energy	16 keV (both Cs^+ and O^-)	generally 8-20 keV (this experiment: 17.1 keV)
analytical signal	mass-to-charge ratio of sputtered ions	X-ray fluorescent photons (XRF)
measurement condition	high vacuum	air or vacuum (+ cryo)
imaging manner	sample position is fixed, ion beam is deflected	X-ray beam is fixed, sample is scanned through X-ray beam
rastering condition	multiple planes, ~1 ms dwell time	one plane, ms–s dwell time
probed depth	few atomic layers	element dependent (µm to mm)
destructiveness of method	atoms are physically ejected	possible radiation damage
multi-element character	up to 7 either positive OR negative ions	yes, if no spectral overlap
element range	from H to U	from Na to U
spatial resolution	• Cs^+ source (non-metals): 50 nm • O^- duoplasmatron (metals): 200 nm • RF source (new prototype): 50 nm • sample/element dependent!	• down to 30 nm • sample-independent
isotopic resolution	Yes	No
sample preparation (for cells)	• Cryofixation, cryosubstitution/embedding + thin sectioning • conducting and flat sample required (e.g. via gold coating)	• also cryofrozen samples possible • no requirement for flat sample!
usual support (for cells)	silicon wafer, polycarbonate filter	silicon nitride membrane
calibration work instrument	source choice, beam alignment, mass selection + optimization	beam alignment, detector optimization
element maps	instantaneous	spectral fitting
availability	• lab instrument, mainly in university context • to be discussed with nano-SIMS facility	• international facility • application form + review process • large oversubscription factor!
cost	generally few k€ for several days of analysis (often based on cost of service contract)	for universities: • travel/lodging costs reimbursed • no analysis cost

Table 1: comparison of nano-SIMS and SR nano-XRF analytical techniques

In this manuscript, the analytical capabilities of nano-SIMS and SR nano-XRF are compared for the specific case of single cell imaging, and the effect of the required sample preparation method upon the elemental distribution is critically investigated. In this way, we want to give the experimenter more insight into which technique can be used best for his/her specific elemental imaging question in single cells, and also indicate some effects of the required sample preparation for both techniques upon the elemental distribution.

For metal imaging with nano-SIMS, an oxygen duoplasmatron source was used in this case study. Although such source is advised for imaging of metal ions, it has lower resolution (min. 200 nm) compared to a cesium source (50 nm) used for imaging of non-metals. Recently, a radiofrequency (RF) oxygen plasma source has become commercially available reaching approx. 40 nm resolution and 5-45 times higher sensitivity for electropositive elements [28]. However, very few of these RF oxygen sources are currently available, and their additional purchase is expensive. Taking this into account, metal imaging only using the oxygen duoplasmatron source was explored in this work. All synchrotron nano-XRF experiments on the other hand were performed at the European Synchrotron Radiation Facility (ESRF). Initially at the ID22NI beamline, a high flux X-ray nanoprobe (currently decommissioned) and its new successor the ID16A 'Nano-Imaging' beamline, currently providing the world's brightest X-ray nanobeam (flux 10^{11} photons/s and 50 nm beam size) and additionally equipped with a state-of-the-art cryogenic sample environment, maintaining cryofrozen samples at 150 K [20].

For practical reasons, the comparison between the different techniques is illustrated on one specific cell type: polymorphonuclear neutrophils (or PMNs), circulating short-lived cells of the innate immune system with a large antimicrobial arsenal and serve as a first line of defense against pathogens [21, 22]. One of these defense mechanisms is the formation of neutrophil extracellular traps (or NETs), in which pathogens get ensnared and killed [23-27]. We were able to compare elemental distributions in high pressure frozen, cryo-substituted and thin-sectioned PMNs using nano-SIMS and nano-XRF under ambient temperature. The obtained elemental distributions were also compared with SR nano-XRF scanning of whole, cryogenically frozen PMNs measured at the ESRF's ID16A beamline.

Results and Discussion

Nano-SIMS imaging of high pressure frozen, cryosubstituted human neutrophils (PMNs).

Fig 1a shows a light microscopy image of the 500 nm thin slabs of embedded PMNs deposited on a silicon chip of 5x5mm². To enable the analysis, PMNs were first vitrified using high pressure freezing (HPF), followed by cryo-substitution in Spurr's resin, which is a mixture of organics containing hydrogen, carbon, but also oxygen and nitrogen [28]. Afterwards, the resin samples were thin-sectioned using a microtome (see Materials and Methods section for more information). A quasi-circular slab is visible in Fig 1a, containing hundreds of neutrophils visible as small, pink dots. From the Spurr's resin cube, 70 nm thin sections were cut for transmission electron microscopy (TEM) imaging. Fig 1b shows a TEM image of a single, randomly chosen PMN located within the 70 nm section, adjacent to the 500 nm thin section used for nano-SIMS analysis. The two darker regions are part of the lobulated nucleus, while the white space between nucleus and cytoplasm has likely been caused by artefacts from the HPF and/or chemical fixation. The denser the structure (i.e. the nucleus in this case), the less water it contains and the better the cryofixation (due to less formation of ice crystals). On the other hand, denser structures sometimes require more time to allow the resin to penetrate the tissue. For this specific case, no ice crystals are visible and the artefact is likely caused by osmotic pressure differences between nucleus and cytoplasm. The latter can be solved by changing infiltration times and/or an adapted cryoprotectant [29].

The white rectangle in Fig 1a indicates the PMN which was imaged by nanoSIMS. NanoSIMS imaging was performed at Utrecht University using the NanoSIMS 50L instrument (Cameca) equipped with a cesium and oxygen duoplasmatron source. Pure silicon wafers were used as substrate for the 500 nm thin sample slabs (adjacent to the 70 nm sections used for TEM imaging) since they avoid charging, are readily available, strong and cheap. In general, we observed better quality of nano-SIMS images after the thin sample resin slabs were pre-sputtered with the cesium source. This process implants cesium atoms into the sample, which leads to higher secondary ion yields and thus better signal-to-noise ratio. Fig 1c shows isotopic maps of ^{12}C, ^{16}O, $^{12}C^{14}N$, ^{31}P, ^{32}S and ^{34}S of the PMN indicated in Fig 1a, measured using the nano-SIMS cesium(Cs)-source. Note that when using the nano-SIMS Cs-source, elements such as C, O and N can all be imaged, privileging this source to investigate lighter elements when of interest. The basic morphology of the PMN cell is clearly recognizable in the maps of ^{12}C, ^{16}O and $^{12}C^{14}N$. Although the size of a single pixel in the isotope maps is 20 nm, the actual resolution was estimated at approx. 200 nm/pixel (more accurate estimations of the resolution were not performed as this was considered

beyond the available time and scope of this study). Note also that spatial imaging resolution obtained with nano-SIMS is sample-dependent, meaning that better conducting samples typically provide higher imaging resolution. Interestingly, regions containing the highest $^{12}C^{14}N$ ion counts also appear darkest in the TEM image in Fig 1b, indicating their lower electron density. Due to the presence of phosphorus-containing DNA in the lobulated nucleus of the PMNs, ^{31}P is strongly present there. Smaller granules in the cytoplasm seem to be rich in ^{32}S, ^{34}S and $^{12}C^{14}N$, indicating their sulphur- and nitrogen-rich protein content; the presence of sulphur-rich proteins within antimicrobial granules has indeed been reported for PMNs [30, 31]. More phosphorous is present on the outer, i.e. perinuclear region of the nucleus, characterized at the same time by less sulphur. A $^{12}C^{14}N$- and ^{32}S-poor and ^{12}C rich region is also present between nucleus and cytoplasm (indicated with a white arrow in Fig 1c), which we believe to be an result from the Spurr's resin infiltration.

Imaging of metals requires bombardment of the sample surface with negative ions. Therefore, the cesium source was first exchanged to the available oxygen duoplasmatron source and the instrument was tuned to allow the detection of biologically relevant metals ^{39}K, ^{40}Ca, ^{55}Mn, ^{56}Fe, ^{63}Cu and ^{64}Zn. Since the supporting wafer was made from pure silicon, the ^{28}Si isotope was monitored as well. Another PMN from control culture was scanned, located on the same thin section as the PMN shown in Fig 1a. The results of metal imaging on the PMN with the duoplasmatron source are shown in Fig 1d. Note that to image two possible PMN candidate cells simultaneously, the field of view is twice as large as in Fig 1c (i.e. 20x20 μm^2 instead of 10x10 μm^2). Unfortunately, a significantly lower spatial resolution is obtained when deploying the oxygen source (Fig 1d) compared to the cesium source (Fig 1c). In Fig 1d, isotope maps of ^{28}Si, ^{39}K, ^{40}Ca, ^{56}Fe, ^{55}Mn, ^{56}Fe and ^{63}Cu all show two spherical structures which, given their size, likely represent entire neutrophil cells. Although the (trace level) ^{56}Fe isotopic map still provides an acceptable signal-to-noise ratio, ^{55}Mn, ^{63}Cu and ^{64}Zn are close to the limit of detection (LOD). For obtaining more depth information, hundred planes were measured overnight, which did not provide significant additional information. As already mentioned in the introduction, an RF oxygen plasma source has been recently developed reaching approx. 40 nm resolution and 5-45 times higher sensitivity for electropositive elements which would provide superior metal imaging capability compared to the oxygen duoplasmatronsource used in our case [32]. Due to the limited availability of this source and its high cost, this option was not explored within this work.

Fig 1 [IN COLOR]: a) microscope image of a 500 nm thin slab of Spurr's resin containing hundreds of single PMNs from control culture. Region indicated with a white rectangle indicates the PMN scanned with nano-SIMS. b) TEM image of a single PMN from the same control culture c) distribution of ^{12}C, ^{16}O, $^{12}C^{14}N$, ^{28}Si, ^{31}P, Esi (electron secondary ionization), ^{32}S, ^{34}S in a single PMN from control culture (cesium source, 10x10 µm², 512x512 pixels, 20 nm/pixel, 100 planes, 2 pA, pre-sputtered for 15 min with 10 pA), the cell membrane of the PMN is indicated with a white dashed line, d) distribution of ^{28}Si, ^{39}K, ^{40}Ca, ^{56}Fe, ^{55}Mn, ^{63}Cu, ^{64}Zn (oxygen duoplasmatron source, 200 pA, 20x20 µm², 256x256 pixels, 80 nm/pixel, 157 planes, no pre-sputtering). In c) and d), natural abundance of the measured isotope is given in the lower left corner of each map. Color bar on the right hand side represents secondary ion counts; min. and max. intensity value is provided above each isotope map (between square brackets).

Fig 2 shows TEM and nano-SIMS imaging of control culture PMNs and PMNs releasing so-called neutrophil extracellular traps (NETs), which are recently discovered fibrous structures in which pathogens get ensnared and killed [23-27]. NETs are of interest for elemental imaging as they potentially contain proteins harvesting metals from pathogens [26, 33-35]. Under *in vitro* conditions, NET-formation can be induced using PMA (phorbol myristate acetate). In our study, PMN cell cultures were exposed to PMA for 1 h and 2 h and then high pressure frozen at specific time intervals in a reverse-time course series. Due to the lower resolution and sensitivity of the oxygen source, stimulated PMNs were investigated with nano-SIMS using the cesium source only. Electron multiplier detectors of the nano-SIMS were optimized for the following isotopes: ^{12}C, ^{16}O, $^{12}C^{14}N$, ^{31}P, ^{31}S and ^{32}S. Note that in Fig 1, nano-SIMS isotope maps of a single PMN from control culture are already provided once and that Fig 2a shows measurements upon another PMN from the same control culture. As in Fig 1, phosphorus is strongly present in the perinuclear region and sulfur is present as granules within the cytoplasm. A $^{12}C^{14}N$, ^{31}P, and ^{32}S-poor and ^{12}C, ^{16}O-rich region (indicated with white arrow) is also present between nucleus and cytoplasm, which we hypothesize to be a sample preparation artefact caused by differential migration of the resin into the cell (see previous paragraph). Note that in comparison with Fig 1, ^{16}O and ^{31}P are affected here as well. Although not performed upon the same cell, PMN morphology obtained via TEM images can be clearly correlated to the nano-SIMS isotopic maps: after 1h PMA stimulation (Fig 2b), one PMN (upper left, indicated with no. 1) remains intact, while the other PMN (indicated with no. 2) seems to have burst open. Although this could represent cell damage during sample preparation, it may also be actual release of the PMNs intracellular content to the extracellular environment, which

may indicate the start of NET formation. Note that due to the limited number of measuring days on the SIMS instrument available and our aim to image several PMNs together, the field of view differs across the different PMA exposure times. In Fib 2c, the TEM image of PMNs stimulated with PMA for 2h (40x40 µm²), the surface area of all PMNs has increased significantly and the different PMNs merged, resulting in nuclei that reside in one common cytoplasm 'pool' containing the antimicrobial sulphur-rich granules. This morphological pattern is also clearly present in the nano-SIMS isotopic map of ^{12}C, ^{16}O, $^{12}C^{14}N$ (and ^{32}S). Note that for the 2h PMA stimulation case - measured at a later stage - also ^{35}Cl isotope was optimized and measured. Therefore, the ^{34}S map has been replaced in Fig 2c with ^{35}Cl isotope, showing it to be predominantly present in the nuclei. For an unknown reason, the ^{16}O and ^{28}Si isotope map reveal hot-spots in PMA stimulated PMNs, not present in the PMNs from control culture. Although during PMA stimulation reactive oxygen species (ROS) are likely formed by PMNs to create a hostile environment for the pathogen [30, 36], the reason for this increased presence of ^{16}O and ^{28}Si is unknown (isobaric interference is very unlikely since the mass resolving power was 11,000). Note that also some inhomogeneity (region indicated with a white arrow) is observed in Fig 2c due to implantation and/or charging effects. In general, across the entire PMA stimulation, nano-SIMS elemental maps could be clearly correlated with TEM imaging obtained from the same sample (Spurr's resin) cube. However, due to the lower imaging resolution of the duoplasmatron source available, metal imaging was not pursued further.

Fig. 2 [IN COLOR]: a) Nano-SIMS and TEM images of PMNs from control culture (upper row), b) PMNs exposed to PMA for 1h (middle row), c) PMNs exposed to PMA for 2h (lower row). Isotopic maps are shown for: ^{12}C, ^{16}O, $^{12}C^{14}N$, ^{31}P, ^{32}S and ^{34}S (^{34}S replaced by ^{35}Cl for 2h PMA stimulation case). Spurr's resin thin section used for TEM (70nm thickness) and for nano-SIMS (500 nm thickness) originate from the same resin cube. Image parameter for the nano-SIMS measurements are: 16x16 µm², 1024x1024 pixels, 16 nm/pixel, 100 planes (control PMNs), 20x20 µm², 256x256 pixels, 80 nm/pixel, 50 planes (1h PMA exposure), 40x40 µm², 512x512 pixels, 80 nm/pixel, 19 planes (2h PMA exposure). Color bar on the right hand side represents secondary ion counts; min. and max. intensity value is provided above each isotope map (between square brackets).

Comparison of nano-SIMS and SR nano-XRF imaging upon high pressure frozen and cryosubstituted PMNs.

In this section, we compare nano-SIMS imaging results on control PMNs using a cesium-source with those obtained via synchrotron nano-XRF performed under ambient temperature and pressure [27, 37]. SR nano-XRF experiments were performed at the former ID22NI 'nano-imaging beamline' at the European Synchrotron Radiation Facility (ESRF) in Grenoble, France [38]. Sections were cut from the same resin cubes as for the nano-SIMS analysis shown in Fig 1. Since XRF is a deeply penetrating technique compared to surface-sensitive nano-SIMS, sections for nano-XRF were cut slightly thicker (2 µm instead of 500 nm), which increases the amount of probed mass and therefore the signal. Sections were deposited on 500 nm thin silicon nitride (Si_3N_4) membranes instead of silicon wafers, which are free of trace metals and generate minimal background. The upper and middle panel of Fig 3 show the comparison of nano-SIMS (a) and SR based nano-XRF imaging (b) on Spurr's resin thin section of a single PMN from control culture, which was high pressure frozen and cryo-substituted. Pixel size of nano-SIMS maps are estimated to be 16 nm/pixel, although true spatial resolution is about 100-200 nm. Pixel size of nano-XRF elemental maps is 50 nm, which is close to the experimentally determined X-ray beam size. Nano-SIMS maps (Fig 3a) provides information on the elements carbon, oxygen and nitrogen, which cannot be probed with XRF under any circumstance. Light elements like P, S and Cl can however also be probed via nano-XRF (see Fig 3b). SR nano-XRF elemental maps are presented here in counts (300 ms dwell time/pixel). Note that quantification of nano-SIMS elemental maps is still considered difficult to put into practice due to differences that occur between standard and sample.

In Fig 3a, we observe a higher sensitivity for the elements phosphorus and sulphur using nano-SIMS, which is likely due to the absorption of fluorescence within the Spurr's resin and the succeeding air path when using nano-XRF (Fig 3b). Measuring the sections using SR nano-XRF under vacuum conditions would improve this issue, but was not available for this particular instrument (ID22NI). Also note that for lower atomic number elements (e.g. P, S), elemental maps obtained by nano-XRF only have few µm probing depth and are in essence more representative for the surface of the sample, and therefore likely more similar (but not identical) to nano-SIMS isotopic maps. Interestingly, sulphur is not visible anymore in the cytoplasm of the PMNs measured using SR nano-XRF maps (Fig 3b), which can only be caused by lower sensitivity or an effect of the sample preparation. In Fig 3b, elemental information for (trace level) metals K, Ca, Mn, Fe, Co, Ni, Cu and Zn with 50 nm step size and trace level sensitivity is presented, which was not achievable with nano-SIMS oxygen duoplasmatron source, stressing the unique capability

of SR nano-XRF for trace level imaging in single cells (disregarding the capabilities of a SIMS RF oxygen source, which was not used/available in this work). Also note that a larger number of elements - only limited by spectral overlap - is probed, compared to the standard seven isotopes with nano-SIMS. Also higher atomic number elemental maps of biologically relevant non-metals can be probed, such as bromine and iodine. Although this paragraph provides a clear comparison between analytical capabilities of nano-SIMS and SR based nano-XRF of HPF and cryosubstituted PMNs under ambient conditions, question remains whether metal distributions are preserved using this sample preparation method, which will be addressed in next section.

Fig. 3 [IN COLOR]: Comparison of a) nano-SIMS measurements performed under ambient temperature upon high pressure frozen, cryo-substituted PMNs, embedded in Spurr's resin and cut into 500 nm thin section (pixel size 16 nm, approx. 100-200 nm 'true' spatial resolution). Color bar on the right hand side represents secondary ion counts; min. and max. intensity value is provided above each isotope map (between square brackets). b) SR nano-XRF measurements performed under ambient temperature and pressure upon high pressure frozen, cryo-substituted PMNs, embedded in Spurr's resin and cut into 2 µm thin sections (dwell time 300 ms, 50 nm pixel size, expressed as raw counts) 3) SR nano-XRF upon cryofrozen (vitrified) PMNs using automated blotting and plunge freezing (dwell time ms, 50 nm pixel size, expressed in ng/cm² (square-rooted values concentration values are provided for better contrast of the elements Ca, Fe, Zn). PMN cell and nucleus boundary is indicated with a dashed and dotted line, respectively.

Comparison of nano-SIMS imaging on cryosubstituted thin sections with SR based nano-XRF on entire, cryofrozen PMNs

In order to validate the extent to which the embedded samples are representative of the real-life case, PMNs were also measured under cryogenic conditions using SR nano-XRF. Measurements were performed at the newly available ID16NI 'nano-imaging' beamline, which is equipped with a high vacuum, cryogenic sample environment and an entire cryogenic workflow [9, 20]. In contrast to previously shown SIMS/XRF measurements, entire PMNs with variable thickness - instead of thin sections - were measured here since production of micrometer thick vitrified cryosections remains difficult to accomplish [39]. Cell cultures deposited upon a silicon nitride (Si_3N_4) membrane were first

washed, plunge frozen and subsequently analyzed in the frozen-hydrated state, of which the results are are shown in Fig 3c. Quantification of nano-XRF elemental maps was performed via measuring a standard under identical conditions (e.g. AXO Thin Film or NIST SRM 1577C 'bovine liver' and by the Fundamental Parameter (FP) quantification method, including self-absorption correction for the SRM and for the ice layer covering the sample, and background. For more information concerning the XRF quantification method applied, we refer to earlier work [9].

Interestingly, elemental distributions of phosphorus and sulphur in Fig 3c have a higher agreement with the nano-SIMS measurements on cryo-substituted thin sections (Fig 3a) than with the nano-XRF measurements under ambient temperature (Fig 3b). This likely indicates the (partial) preservation of phosphorous and sulphur for the cryo-substitution technique. In Fig 3c, chlorine seems to be clearly more concentrated in the cytoplasm for the cryofrozen PMN, compared to the cryo-substitution case (Fig 3b), suggesting a removal of chlorine during cryo-substitution. Besides these findings for P, S and Cl, nearly all metals (Ca, Mn, Fe, Co, Ni and Zn) are more pronounced in the PMN nucleus measured with nano-XRF under ambient pressure and temperature (Fig 3b). This phenomenon might be caused by the (slightly) higher sensitivity for these elements of SR nano-XRF in-air measurements. For XRF analysis under cryogenic conditions, samples are first blotted after which a (thinner) ice layer remains. The remaining ice layer however still absorbs fluorescence of the lower atomic number elements (P, S, Cl) and also results in increased ice scatter and increased background scatter and fluorescence. In order to illustrate the effect of ice layer thickness upon analytical sensitivity, Fig 4 shows the obtained limits of detections (LODs) in parts-per-million (ppm) and micromolar (μM) calculated from NIST SRM 1577C (bovine liver) measured with nano-XRF under cryogenic conditions. Additionally, the graph shows the LODs which would be obtained when the SRM is covered with 10, 50 and 100 μm of pure ice. From this graph, we clearly see that a covering ice layer of only 10 μm has already a significant effect on the LOD for lower atomic number elements such as P, S and Cl. For heavier elements, starting from manganese here, ice absorption effects are almost negligible. For more information on the calculation of the LODs with the presence of ice, we refer to previous work [9]. Ice absorption effects can be suppressed by better control of a thin ice layer formation or by using collimators on the detector side, rejecting a larger portion of the background scatter and fluorescence. Controlling the thickness of such ice layer remains a difficult task and pre-characterization under cryogenic conditions requires specialized equipment.

Although vitrified samples are considered as close as possible to the real-life condition, some artefacts may still be present due to (manual) plunge freezing, such as the formation ice cracks and/or formation

of ice crystals. Manual plunge freezing is not performed under uniform high pressure (as is the case with HPF), which may result in the formation of ice layers. With respect to the formation of ice crystals, an interesting signal is the Au-L ('gold L-line') fluorescent signal in Fig 3c. This signal actually does not reflect the presence of true gold, but rather the presence of ice crystals/crystallinity in the sample, diffracting X-ray photons upon the gold-coated sample holder used in this set-up, which on its turn emits gold fluorescent photons towards the detector. Although two different beamlines were used for obtaining the results in Fig 3b and Fig 3c, i.e. former ID22NI and its successor ID16A respectively, imaging results can be compared fairly direct as both are high flux nanoprobes (10^{11} photons/s) with nanoscopic resolution (50 nm), with the difference that sample environment is different (ambient temperature vs cryogenic), as well as the sample thickness (sectioned slabs vs entire cells).

Fig 4 [IN COLOR]: Relative limit of detection (in ppm, left Y-axis) and molar limit of detection (in µmolar or µM, right Y-axis) obtained for NIST SRM 1577c (bovine liver) at beamline ID16NI. LODs were estimated for the SRM only and for different ice layers of 10-50-100 µm covering the SRM (see legend). LODs were determined for typical scanning conditions at ID16NI: 17 keV excitation energy, high-dose mode (2x1011 photons/s), no absorbers in the beam path, 50 ms dwell time and normalized to 200 mA ESRF ring current.

Materials and Methods

Cell culture, High pressure freezing and cryosubstitution

In a 45 µL droplet, $2.5x10^4$ neutrophils in HEPES-buffered RPMI were seeded onto a 1.4 mm sapphire disk (Leica consumables nr. 16706849). To isolate neutrophils from peripheral blood we have acquired venous blood from healthy voluntary donors at the Umeå Blodcentralen with informed written consent in accordance to an ethical permission 09-210M from the regional ethical board in Umeå. All blood samples were taken by trained personnel (not by the authors themselves) and tested negative for HBsAg, HIV 1/2 ab and ag (HIV combo test), anti-HCV and syphilis. The blood samples exclusively served as a source for primary neutrophils. No donor data were used or saved anywhere, nor were any personal data relevant for the study.

NET formation was induced by adding 100 nM PMA or cells were left unstimulated. Stimulated cells were incubated for up to 4 h at 37 °C with 5 % CO_2. Then, the medium was carefully removed, cells were washed twice very briefly with a droplet of ultraclean H_2O and 50 µl of 20 % w/v BSA in PBS were added onto each sapphire disk as a cryoprotectant. The sapphire disc was then inserted in a membrane carrier (Leica consumables nr.16707898, 1.4 mm diameter, 100 µm thickness) and frozen immediately in a high pressure freezer (EM PACT; Leica Microsystems, Vienna, Austria). Freeze substitution was carried out using a Leica EM AFS2 (Leica Microsystems) in dry acetone with 0.1 % glutaraldehyde over 4 days as follows: -90° C per hour increase for 15 hours, and -30°C for 24 hours. Samples were then washed 3 times in pure acetone and slowly warmed up to 4°C, infiltrated stepwise over 3 days at 4°C in Spurr's resin (solution composed of 450 g nonenylsuccinic anhydride (NSA), 250 g ERL 4221, 250 g DER 736 and 100 g dimethylaminoethanol (DMAE) from emsdiasum.com, Hatfield) and embedded in capsules. The polymerization was performed at 70°C for 16h.

For TEM analysis of the prepared samples, ultrathin sections (approx. 60 nm) were cut using an ultramicrotome (Leica EM UC6) and post-stained in a Leica EM AC20 for 40 min in uranyl acetate at 20°C and for 10 min in lead citrate at 20°C. Grids were viewed with a JEM 1010 transmission electron microscope (JEOL, Tokyo, Japan) operating at 80 kV using Image Plate Technology from Ditabis (Pforzheim, Germany).

For nano-SIMS analysis, thin sections of 500 nm and 1 µm made from the Spurr's resin trimmed cube (see above) were deposited on a 5x5mm² silicon chip of 500 µm thickness (4" diameter, 5x5mm diced Silicon Wafer, 270 chips/wafer, Ted pella inc., order no. 16008).

For SR nano-XRF analysis under atmospheric conditions, semi-thin sections (2 µm), were cut and deposited on square silicon nitride (Si_3N_4) ultra-thin membranes in square silicon nitride supporting frames from Silson Ltd, Northampton, UK (3.0 x 3.0 mm membrane size, 500 nm membrane thickness, 7.5 x 7.5 mm frame size and 200 µm frame thickness).

Automated Plunge Freezing

Silicon nitride membrane frames from Silson Ltd (5x5 mm frame size, 1.5x1.5 mm membrane area, 200 µm frame thickness and 500 nm membrane thickness) were rinsed two times in 70 % ethanol and two times in milliQ water before PMNs were cultured as described in previous paragraph 'Cell Culture, High pressure freezing and cryosubstitution'. Then, each wafer was briefly washed via cautious movement through a 0.25 M ammonium formate buffer solution (NH_4HCO_2, 2.5455 g dissolved in 160 mL milliQ

water) for approx. 5 s, which removes the metal-containing medium from the silicon nitride wafers. Both sides of the wafer were then blotted with an automated plunge freezer (Vitrobot™, FEI, The Netherlands) to remove the excess of washing buffer; blotting time was varied between 1-2 s. After cryofication, wafers were put in cryogenic vials with screw caps. Few days before the experiment, samples were shipped to the ESRF using a dryshipper (Cryoport™, US) with continuous registration and on-line readout of temperature, pressure and slope.

Nano-SIMS

Nano-SIMS measurements were performed in June 2017 the CAMECA™ NanoSIMS 50L instrument located at Utrecht University. Silicon chips carrying both 1 µm and 500 nm thin sections were made, but only the 500 nm sections were analyzed with nano-SIMS due to time constraint and better conductivity. Silicon chips were clamped into a nano-SIMS sample holder fabricated for biology purposes using a 5 mm diameter spacer ring. Using the Cs^+ source, electron multiplier detectors were adjusted for the following elements: ^{12}C, ^{16}O, $^{12}C^{14}N$, ^{28}Si, ^{31}P, ^{32}S and ^{34}S. Secondary electron image (ESI) was acquired as well. Typical current of the primary Cs^+ ion beam was 2 pA. ^{28}Si served as detection means for the sample support and for optimization purposes. Mass resolving power (MRP) value of up to 11,000 was obtained. All samples were pre-sputtered using the Cs^+ source with a higher ion current of 10 pA for approx. 15 min. Note that during the pre-sputtering phase, data acquisition is not possible as this would result in detector overload.

With the aim of detecting metals, the instrument was subsequently tuned with the duoplasmatron O^- source. In this mode, electron multiplier detectors were optimized for the following elements: ^{28}Si, ^{39}K, ^{40}Ca, ^{56}Fe, ^{55}Mn, ^{63}Cu, ^{64}Zn. Other potential relevant elements detectable with the duoplasmatron oxygen source included Na, Co, Rb and Sr; elements Ni, Se and Co as well, but the signals were too low. Here, a primary ion beam of 100-200 pA was used, compared to the much lower 2 pA for the cesium source. Since the pre-sputtering was harsher for the oxygen source – ultimately reaching the Si wafer – the pre-sputtering step was omitted in order to be sure not having removed the layer of interest. Analysis of all results was done by the Look@SIMS software package [40]. This package autoscales and aligns all plane images using a base mass for alignment before summing all plane intensities.

SR based nano-XRF analysis under ambient temperature

Non-cryogenic nano-XRF experiment were performed in July 2011 at the former ID22NI beamline located at the European Synchrotron Radiation Facility (ESRF) in Grenoble, France. This instrument was installed at a high-β straight section equipped with two different undulators covering an energy range of 6-70 keV. The ID22NI nanoprobe (currently replaced by the nano-imaging nano-analysis outstation or NINA, see next paragraph) was dedicated to hard X-ray nanoanalysis allowing nano-XRF and absorption/phase contrast nanotomography. X-ray focusing was obtained by a crossed elliptical rhodium (Rh) coated graded-multilayer mirror-pair in the Kirkpatrick-Baez (KB) geometry. X-rays were collected and focused in both vertical and horizontal axis at a glancing angle (<3.5 mrad). The first mirror, coated with a graded multilayer plays both the role of vertical focusing device and monochromator, resulting in a very high flux (10^{12} photons/s) and a medium monochromaticity ($\Delta E/E \approx 10^{-2}$). The beam size was determined by knife-edge scans of a gold (Au) test pattern and determined to be 64 nm vertically and 54 nm horizontally at an excitation energy of 17 keV. For XRF detection, a single Vortex™ silicon drift detector (SDD) with 50 mm² active area and lead collimator was used, placed at a 15° angle with respect to the sample surface and at a distance of approx. 20 mm from the sample. Scans were performed in continuous mode with a dwell time of 50 ms/pixel.

SR nano-XRF experiments under cryogenic conditions

Scanning nano-XRF experiments of cryogenically frozen PMNs were performed at the ID16A-NI (Nano-Imaging) beamline (UPBL04) in February 2017. ID16-NI provides the world's brightest hard X-ray nanofocus, i.e. 2 x 10^{11} photons/s, confined within a beam of 27 nm horizontally by 21 nm vertically full-width at half-maximum (FWHM). Beamline techniques include full field holography, ptychography and X-ray fluorescence. Incident energy upon the X-ray focusing optics housed within the high vacuum sample chamber is 17.1 keV having a spectral bandwidth ΔE/E of 1 %, also 33.6 keV excitation energy can be provided. Measurements are performed in-vacuum and, if desired, under cryogenic conditions. For XRF detection, an array of 6 in-vacuum silicon drift detectors was used (Rayspec Ltd.) equipped with beryllium window (no collimator), providing an active area of approx. 300 mm², placed at 90 degrees with respect to the incoming beam, but in front of the sample plane by a few mm. Typical measuring time was again 50 ms/pixel. Total sum spectrum of all 6 detectors was used for XRF spectral fitting.

Upon the start of the experiment, cryofrozen wafers of interest are transferred into the liquid nitrogen bath of a Leica™ EM VCM (Vacuum Cryo Manipulation System) where they are clamped in a pre-cooled

gold-coated VCT sample holder. The sample holder is then loaded into the Leica™ EM VCT500 (Vacuum Cryo Transfer system). Finally, sample shuttle is attached to the ID16A-NI vacuum chamber and the gold-coated copper cube holding the silicon nitride membrane with deposited PMNs is transferred onto the sample stage of ID16NI beamline. The temperature of the sample holder clamping the sample wafer is continuously monitored and remains constant at approx. -150 °C. For more information on the technical aspects, we refer to another manuscript [20].

Conclusion & Outlook

Synchrotron radiation-based nano-XRF and nano-SIMS are two powerful, label-free methods for elemental imaging at the nanoscale, both recently reaching the 30 nanometer level. Nano-SIMS has the routine capability of non-metal isotopic imaging (C, N, O, P, S) of main constituents in single cells using a cesium source at the 50 nm level. By the use of a conventional duoplasmatron source, also metals (Mn, Fe, Ni, Cu, Zn) can be mapped at moderate resolution (200-500 nm). Samples however need to be flat and analyzed in high-vacuum. High pressure freezing (HPF), followed by cryo-substitution and resin (e.g. Spurr's resin) embedding is the method par excellence for ultrastructural imaging using transmission electron microscopy (TEM) – another in-vacuum technique - as it preserves the morphological ultrastructure.

First, by measuring thin sections of single cells (human neutrophils), originating from the same Spurr's resin cube, but having different thicknesses, both SR based nano-XRF (performed under ambient temperature and pressure) and nano-SIMS could be compared from the analytical point of view. Generally, we found that nano-SIMS is complementary to nano-XRF as it enables nanoscale (100 nm) mapping of isotopic of elements such as C, O and N which are not accessible with nano-XRF. Nano-XRF, on the other hand, shows its superiority for trace level metal imaging of elements as Ca, Mn, Fe, Ni, Cu and Zn (disregarding the capabilities of a newly developed oxygen RF source). Elemental distributions obtained by nano-XRF/SIMS (e.g. for phosphorus and sulphur) may differ, not only due to sample preparation artefacts, but also due to inherent differences between both analytical techniques: nano-SIMS probes the upper surface layer of the sample (few nm), whereas nano-XRF has increasing probing depth with increasing atomic number (e.g. few µm for phosphorus, several mm for zinc). When operated in air, absorption of X-ray fluorescence of lower atomic number elements (e.g. phosphorus, sulphur) may render their analysis impossible, making then in-vacuum nano-SIMS the more reliable option.

Little is known on the chemical preservation of high pressure frozen and subsequently cryo-substituted cells. The recently enabled SR nano-XRF analysis of single cells in their vitrified, cryofrozen state is likely the method analyzing cells closest to their real-life condition (although cryofixation itself may also cause minor artefacts). Comparison of elemental distributions of high pressure frozen and cryo-substituted cells with cryofrozen cells has therefore only become available now and was practically investigated here. For our particular case study on human neutrophils (PMNs), we found large similarities for the

elements phosphorous and sulphur for both methods, indicating a (partial) preservation of these elements using HPF/cryo-substitution. Likely sulphur and phosphorous are more chemically bound to the cell structure, making them less susceptible to migration during the substitution process. Potassium and chlorine were more pronounced in cryofrozen PMNs compared to PMNs embedded in Spurr's resin, indicating significant removal of these elements after cryo-substitution. On the other hand, thin sections of PMNs measured with SR nano-XRF under ambient temperature showed higher relative intensity of (trace level) metals Ca, Mn, Fe, Ni and Zn in the nucleus, which is likely no sample preparation artefact, but is inflicted by the higher sensitivity of nano-XRF under non-cryogenic conditions, suffering less from X-ray scatter and increased background. All these findings on the effect of sample preparation were obtained on a representative number of cells, using both SR nano-XRF and nano-SIMS techniques.

Recently, an oxygen plasma sources based on a radiofrequency (RF) field has been developed reaching 40 nm resolution and 5-45 times higher sensitivity for electropositive elements, creating new possibilities for trace level metal imaging using nano-SIMS. Further experiments are required to explore the potential of this new source for imaging trace metals like Mn, Fe, Cu and Zn in single cells. The necessity of nano-SIMS to measure cells in a high vacuum environment, requiring sample embedding remains however a weak point. The current gold standard for nanochemical imaging of trace metals in single cells close to the native state remains thus SR nano-XRF equipped with a cryogenic sample environment. It is expected however that nano-SIMS will soon follow in the transition from the analysis of embedded cells towards analysis of cell cryosections in the next decade. Also here, certain issues will need to be addressed, such as cryogenic sample transfer and ice covering the sample. In general, we can state that SR nano-XRF and nano-SIMS stand side-by-side in elemental analysis as two supplementary analytical techniques, each with their own pros and cons. Where SR nano-XRF has the advantage of in-depth analysis, (ultra)trace level metal sensitivity, sample-independent nanoscopic resolution and ability to measure cryofrozen samples, nano-SIMS has the advantage of mapping isotopes, detecting light elements and fast repetitive mapping.

ACKNOWLEDGEMENTS

Björn De Samber acknowledges his postdoctoral research grant from FWO Vlaanderen (www.fwo.be, application no. 12B3313N). The NanoSIMS facility at Utrecht University was financed through a large infrastructure grant by the Netherlands Organisation for Scientific Research (NWO) awarded to Jack Middelburg (grant no. 175.010.2009.011). Constantin Urban acknowledges funding from the Swedish Research Council VR-MH 2017-01681.

DATA AVAILABILITY STATEMENT

The ESRF Council has recently endorsed the implementation of a Data Policy for data taken at the ESRF beamlines. The Data Policy is based on the PaNdata Data Policy which was a deliverable of the European FP7 project PaN-data Europe (http://pan-data.eu/) delivered in 2011. The Data Policy defines the ESRF as the custodian of raw data and metadata. The metadata is stored in the ICAT metadata catalogue (https://icatproject.org/) which can be accessed online (https://icat.esrf.fr) to browse and download (meta)data. The metadata will be stored in the ICAT metadata catalogue which can be accessed online to browse and download (meta)data. A three-year embargo period applies after each ESRF measurement during which the experimental team has the right to have sole access to the data, renewable if necessary. The (meta) data related to the experiment of this manuscript (LS-2550) performed in February 2017 will therefore be released entirely in February 2020 under a CC-BY-4 license with open access to anyone who has registered with the ESRF data portal.

References

[1] P.L. Clode, R.A. Stern, A.T. Marshall, Subcellular imaging of isotopically labeled carbon compounds in a biological sample by ion microprobe (NanoSIMS), Microsc. Res. Tech., 70 (2007) 220-229.

[2] A. Delaune, A. Cabin-Flaman, G. Legent, D. Gibouin, C. Smet-Nocca, F. Lefebvre, A. Benecke, M. Vasse, C. Ripoll, 50nm-Scale Localization of Single Unmodified, Isotopically Enriched, Proteins in Cells, PLoS One, 8 (2013) 12.

[3] C. Guillermier, M.L. Steinhauser, C.P. Lechene, Quasi-simultaneous acquisition of nine secondary ions with seven detectors on NanoSIMS50L: application to biological samples, Surface and Interface Analysis, 46 (2014) 150-153.

[4] C. Lechene, F. Hillion, G. McMahon, D. Benson, A.M. Kleinfeld, J.P. Kampf, D. Distel, Y. Luyten, J. Bonventre, D. Hentschel, K.M. Park, S. Ito, M. Schwartz, G. Benichou, G. Slodzian, High-resolution quantitative imaging of mammalian and bacterial cells using stable isotope mass spectrometry, Journal of biology, 5 (2006) 20.

[5] R.F.S. Lee, T. Riedel, S. Escrig, C. Maclachlan, G.W. Knott, C.A. Davey, K. Johnsson, A. Meibom, P.J. Dyson, Differences in cisplatin distribution in sensitive and resistant ovarian cancer cells: a TEM/NanoSIMS study, Metallomics, 9 (2017) 1413-1420.

[6] C. Quintana, T.D. Wu, B. Delatour, M. Dhenain, J.L. Guerquin-Kern, A. Croisy, Morphological and chemical studies of pathological human and mice brain at the subcellular level: Correlation between light, electron, and NanoSIMS microscopies, Microsc. Res. Tech., 70 (2007) 281-295.

[7] A. Carmona, P. Cloetens, G. Deves, S. Bohic, R. Ortega, Nano-imaging of trace metals by synchrotron X-ray fluorescence into dopaminergic single cells and neurite-like processes, Journal of Analytical Atomic Spectrometry, 23 (2008) 1083-1088.

[8] S. Corezzi, L. Urbanelli, P. Cloetens, C. Emiliani, L. Helfen, S. Bohic, F. Elisei, D. Fioretto, Synchrotron-based X-ray fluorescence imaging of human cells labeled with CdSe quantum dots, Anal. Biochem., 388 (2009) 33-39.

[9] B. De Samber, E. Meul, B. Laforce, B. De Paepe, J. Smet, M. De Bruyne, R. De Rycke, S. Bohic, P. Cloetens, R. Van Coster, P. Vandenabeele, T. Vanden Berghe, Nanoscopic X-ray fluorescence imaging and quantification of intracellular key-elements in cryofrozen Friedreich's ataxia fibroblasts, PLoS One, 13 (2018) 24.

[10] R. Ortega, P. Cloetens, G. Deves, A. Carmona, S. Bohic, Iron Storage within Dopamine Neurovesicles Revealed by Chemical Nano-Imaging, PLoS One, 2 (2007) 6.

[11] C. Sanchez-Cano, I. Romero-Canelon, Y. Yang, I.J. Hands-Portman, S. Bohic, P. Cloetens, P.J. Sadler, Synchrotron X-Ray Fluorescence Nanoprobe Reveals Target Sites for Organo-Osmium Complex in Human Ovarian Cancer Cells, Chem.-Eur. J., 23 (2017) 2512-2516.

[12] B. De Samber, K.A.C. De Schamphelaere, C.R. Janssen, B. Vekemans, R. De Rycke, G. Martinez-Criado, R. Tucoulou, P. Cloetens, L. Vincze, Hard X-ray nanoprobe investigations of the subtissue metal distributions within Daphnia magna, Anal. Bioanal. Chem., 405 (2013) 6061-6068.

[13] B. De Samber, M.J. Niemiec, B. Laforce, J. Garrevoet, E. Vergucht, R. De Rycke, P. Cloetens, C.F. Urban, L. Vincze, Probing Intracellular Element Concentration Changes during Neutrophil Extracellular Trap Formation Using Synchrotron Radiation Based X-Ray Fluorescence, PLoS One, 11 (2016).

[14] J.F. Collingwood, F. Adams, Chemical imaging analysis of the brain with X-ray methods, Spectroc. Acta Pt. B-Atom. Spectr., 130 (2017) 101-118.

[15] D. Studer, M. Michel, M. Muller, HIGH-PRESSURE FREEZING COMES OF AGE, Scanning Microsc., (1989) 253-269.

[16] D. Studer, W. Graber, A. Al-Amoudi, P. Eggli, A new approach for cryofixation by high-pressure freezing, Journal of Microscopy, 203 (2001) 285-294.

[17] G.F. Zhang, L.A. Staehelin, FUNCTIONAL COMPARTMENTATION OF THE GOLGI-APPARATUS OF PLANT-CELLS - IMMUNOCYTOCHEMICAL ANALYSIS OF HIGH-PRESSURE FROZEN-SUBSTITUTED AND FREEZE-SUBSTITUTED SYCAMORE MAPLE SUSPENSION-CULTURE CELLS, Plant Physiol., 99 (1992) 1070-1083.
[18] L.A. Staehelin, T.H. Giddings, J.Z. Kiss, F.D. Sack, MACROMOLECULAR DIFFERENTIATION OF GOLGI STACKS IN ROOT-TIPS OF ARABIDOPSIS AND NICOTIANA SEEDLINGS AS VISUALIZED IN HIGH-PRESSURE FROZEN AND FREEZE-SUBSTITUTED SAMPLES, Protoplasma, 157 (1990) 75-91.
[19] S. Chen, J. Deng, Y. Yuan, C. Flachenecker, R. Mak, B. Hornberger, Q. Jin, D. Shu, B. Lai, J. Maser, C. Roehrig, T. Paunesku, S.C. Gleber, D.J. Vine, L. Finney, J. VonOsinski, M. Bolbat, I. Spink, Z. Chen, J. Steele, D. Trapp, J. Irwin, M. Feser, E. Snyder, K. Brister, C. Jacobsen, G. Woloschak, S. Vogt, The Bionanoprobe: hard X-ray fluorescence nanoprobe with cryogenic capabilities, J. Synchrot. Radiat., 21 (2014) 66-75.
[20] J.C. Da Silva, A. Pacureanu, Y. Yang, S. Bohic, C. Morawe, R. Barrett, P. Cloetens, Efficient concentration of high-energy x-rays for diffraction-limited imaging resolution, Optica, 4 (2017) 492-495.
[21] N. Borregaard, Neutrophils, from Marrow to Microbes, Immunity, 33 (2010) 657-670.
[22] W.M. Nauseef, N. Borregaard, Neutrophils at work, Nature Immunology, 15 (2014) 602-611.
[23] V. Brinkmann, U. Reichard, C. Goosmann, B. Fauler, Y. Uhlemann, D.S. Weiss, Y. Weinrauch, A. Zychlinsky, Neutrophil extracellular traps kill bacteria, Science, 303 (2004) 1532-1535.
[24] V. Brinkmann, A. Zychlinsky, Beneficial suicide: why neutrophils die to make NETs, Nat. Rev. Microbiol., 5 (2007) 577-582.
[25] Q. Remijsen, T.W. Kuijpers, E. Wirawan, S. Lippens, P. Vandenabeele, T. Vanden Berghe, Dying for a cause: NETosis, mechanisms behind an antimicrobial cell death modality, Cell Death Differ., 18 (2011) 581-588.
[26] C.F. Urban, D. Ermert, M. Schmid, U. Abu-Abed, C. Goosmann, W. Nacken, V. Brinkmann, P.R. Jungblut, A. Zychlinsky, Neutrophil Extracellular Traps Contain Calprotectin, a Cytosolic Protein Complex Involved in Host Defense against Candida albicans, Plos Pathogens, 5 (2009) 18.
[27] M.J. Niemiec, B. De Samber, J. Garrevoet, E. Vergucht, B. Vekemans, R. De Rycke, E. Bjorn, L. Sandblad, G. Wellenreuther, G. Falkenberg, P. Cloetens, L. Vincze, C.F. Urban, Trace element landscape of resting and activated human neutrophils on the sub-micrometer level, Metallomics, 7 (2015) 996-1010.
[28] L.C.P.W. R.R., Microbeam Analysis in Biology, Academic Press, Inc. (LONDON) LTD.1979.
[29] d.R.D. Rycke, Personal communication.
[30] F.C. Fang, Antimicrobial reactive oxygen and nitrogen species: Concepts and controversies, Nat. Rev. Microbiol., 2 (2004) 820-832.
[31] T. Nakatsuji, R.L. Gallo, Antimicrobial peptides: Old Molecules with New Ideas, The Journal of investigative dermatology, 132 (2012) 887-895.
[32] J. Malherbe, F. Penen, M.P. Isaure, J. Frank, G. Hause, D. Dobritzsch, E. Gontier, F. Horreard, F. Hillion, D. Schaumloffel, A New Radio Frequency Plasma Oxygen Primary Ion Source on Nano Secondary Ion Mass Spectrometry for Improved Lateral Resolution and Detection of Electropositive Elements at Single Cell Level, Analytical Chemistry, 88 (2016) 7130-7136.
[33] I. Striz, I. Trebichavsky, Calprotectin - a pleiotropic molecule in acute and chronic inflammation, Physiological research, 53 (2004) 245-253.
[34] T.E. Kehl-Fie, S. Chitayat, M.I. Hood, S. Damo, N. Restrepo, C. Garcia, K.A. Munro, W.J. Chazin, E.P. Skaar, Nutrient Metal Sequestration by Calprotectin Inhibits Bacterial Superoxide Defense, Enhancing Neutrophil Killing of Staphylococcus aureus, Cell Host Microbe, 10 (2011) 158-164.
[35] T.G. Nakashige, B. Zhang, C. Krebs, E.M. Nolan, Human calprotectin is an iron-sequestering host-defense protein, Nat Chem Biol, 11 (2015) 765-771.

[36] S.J. Dixon, B.R. Stockwell, The role of iron and reactive oxygen species in cell death, Nat. Chem. Biol., 10 (2014) 9-17.
[37] B. De Samber, M.J. Niemiec, B. Laforce, J. Garrevoet, E. Vergucht, R. De Rycke, P. Cloetens, C.F. Urban, L. Vincze, Probing Intracellular Element Concentration Changes during Neutrophil Extracellular Trap Formation Using Synchrotron Radiation Based X-Ray Fluorescence, PLoS One, 11 (2016) e0165604.
[38] G. Martinez-Criado, R. Tucoulou, P. Cloetens, P. Bleuet, S. Bohic, J. Cauzid, I. Kieffer, E. Kosior, S. Laboure, S. Petitgirard, A. Rack, J.A. Sans, J. Segura-Ruiz, H. Suhonen, J. Susini, J. Villanova, Status of the hard X-ray microprobe beamline ID22 of the European Synchrotron Radiation Facility, J. Synchrot. Radiat., 19 (2012) 10-18.
[39] J. Pierson, J.J. Fernandez, E. Bos, S. Amini, H. Gnaegi, M. Vos, B. Bel, F. Adolfsen, J.L. Carrascosa, P.J. Peters, Improving the technique of vitreous cryo-sectioning for cryo-electron tomography: Electrostatic charging for section attachment and implementation of an anti-contamination glove box, J. Struct. Biol., 169 (2010) 219-225.
[40] L. Polerecky, B. Adam, J. Milucka, N. Musat, T. Vagner, M.M.M. Kuypers, Look@NanoSIMS - a tool for the analysis of nanoSIMS data in environmental microbiology, Environ. Microbiol., 14 (2012) 1009-1023.

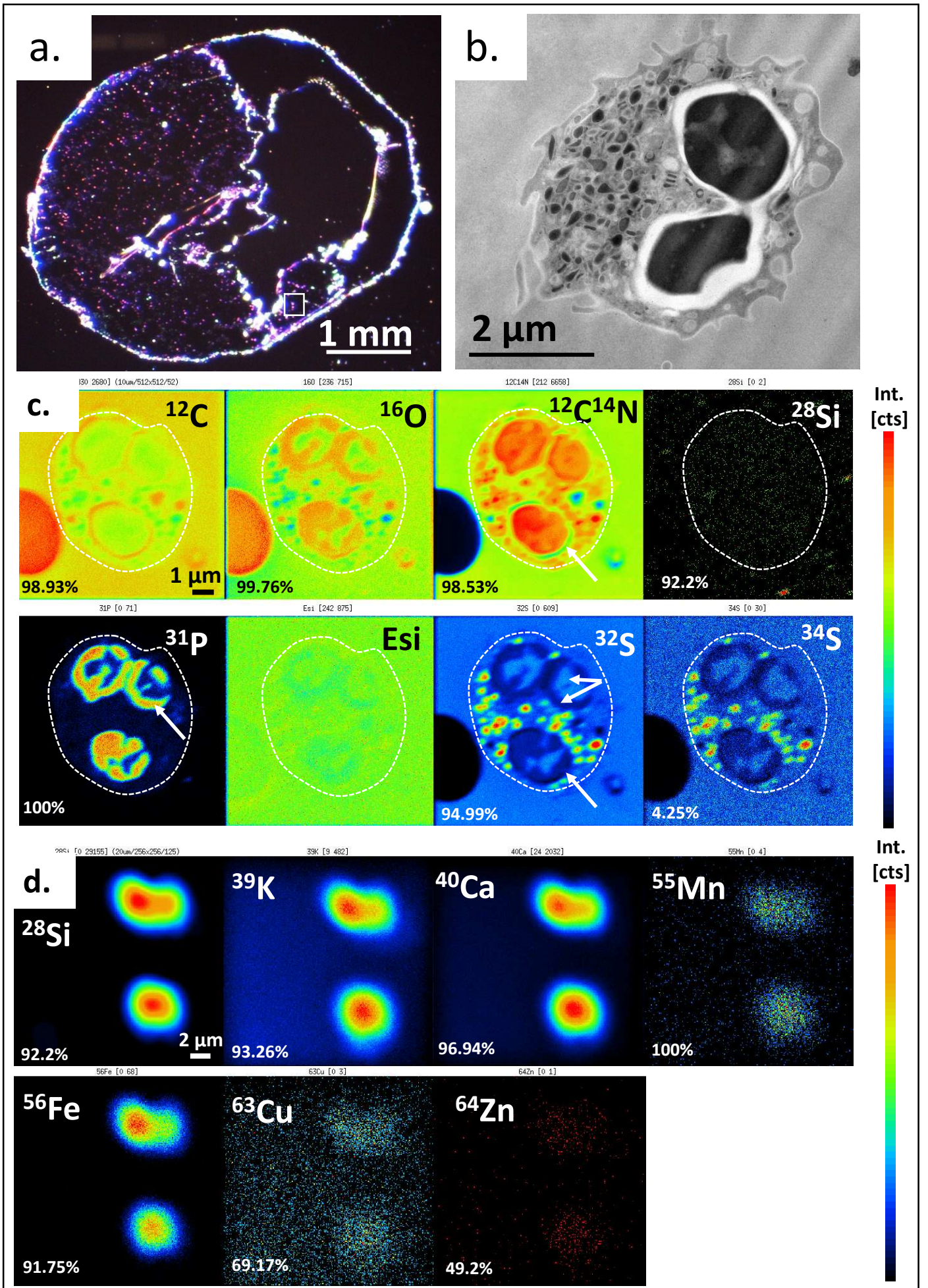
a.
1 mm
b.
2 µm
c.
12C
16O
12C14N
28Si
98.93%
1 µm
99.76%
98.53%
92.2%
31P
Esi
32S
34S
100%
94.99%
4.25%
Int. [cts]
d.
28Si
39K
40Ca
55Mn
92.2%
2 µm
93.26%
96.94%
100%
56Fe
63Cu
64Zn
91.75%
69.17%
49.2%
Int. [cts]

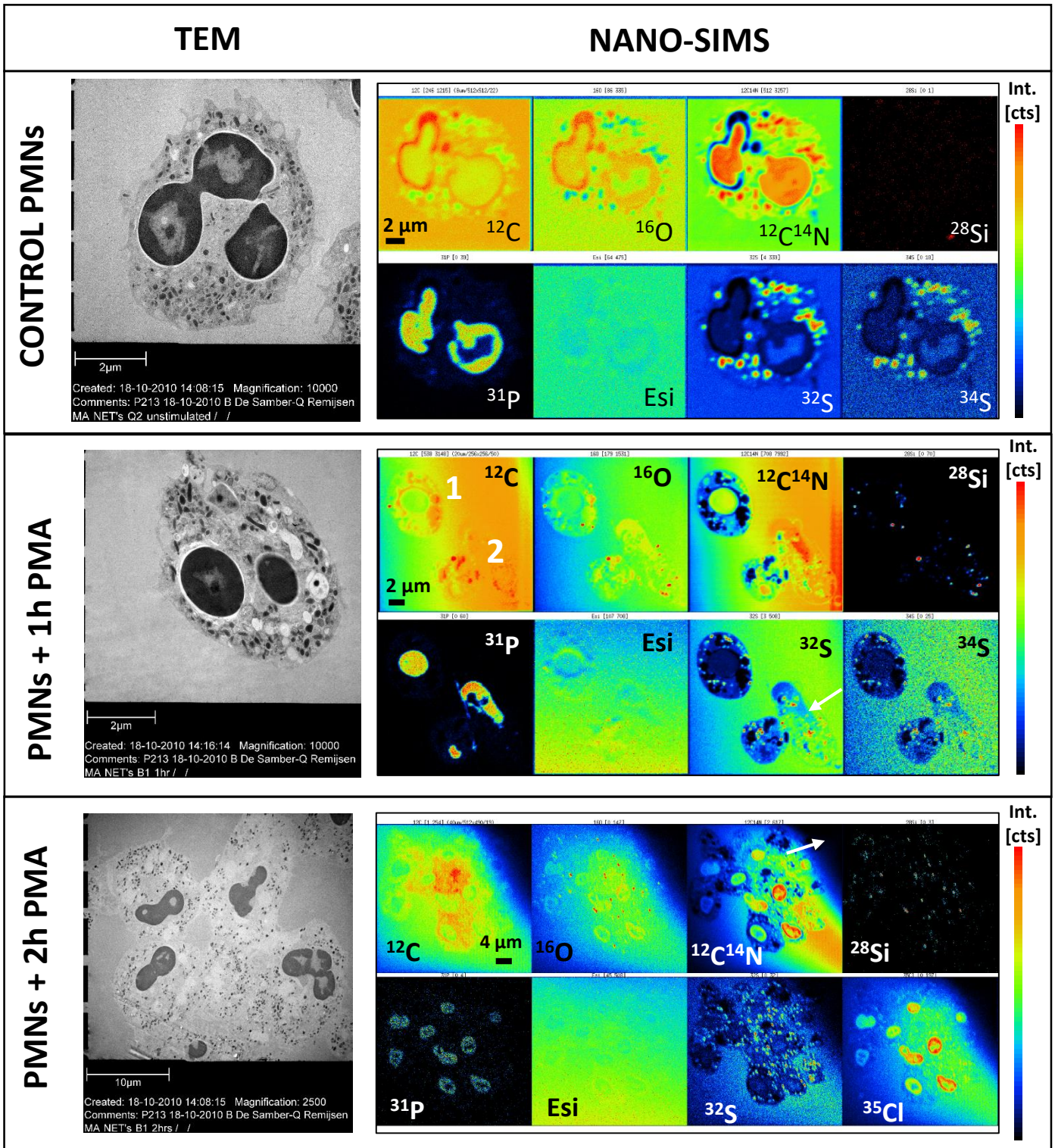
TEM
NANO-SIMS
CONTROL PMNs
2µm
Created: 18-10-2010 14:08:15 Magnification: 10000
Comments: P213 18-10-2010 B De Samber-Q Remijsen
MA NET's Q2 unstimulated / /
2 µm
12C
16O
12C14N
28Si
31P
Esi
32S
34S
Int. [cts]
PMNs + 1h PMA
2µm
Created: 18-10-2010 14:16:14 Magnification: 10000
Comments: P213 18-10-2010 B De Samber-Q Remijsen
MA NET's B1 1hr / /
1
2
2 µm
12C
16O
12C14N
28Si
31P
Esi
32S
34S
Int. [cts]
PMNs + 2h PMA
10µm
Created: 18-10-2010 14:08:15 Magnification: 2500
Comments: P213 18-10-2010 B De Samber-Q Remijsen
MA NET's B1 2hrs / /
4 µm
12C
16O
12C14N
28Si
31P
Esi
32S
35Cl
Int. [cts]

a)

NANO-SIMS

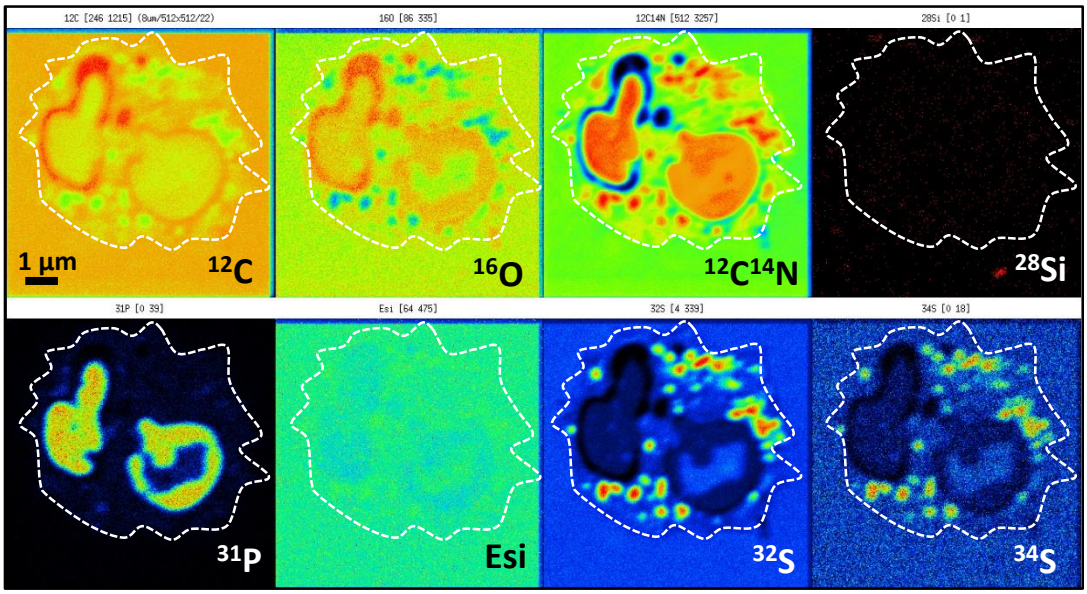

b)

NANO-XRF (HPF/CRYOSUBST.)

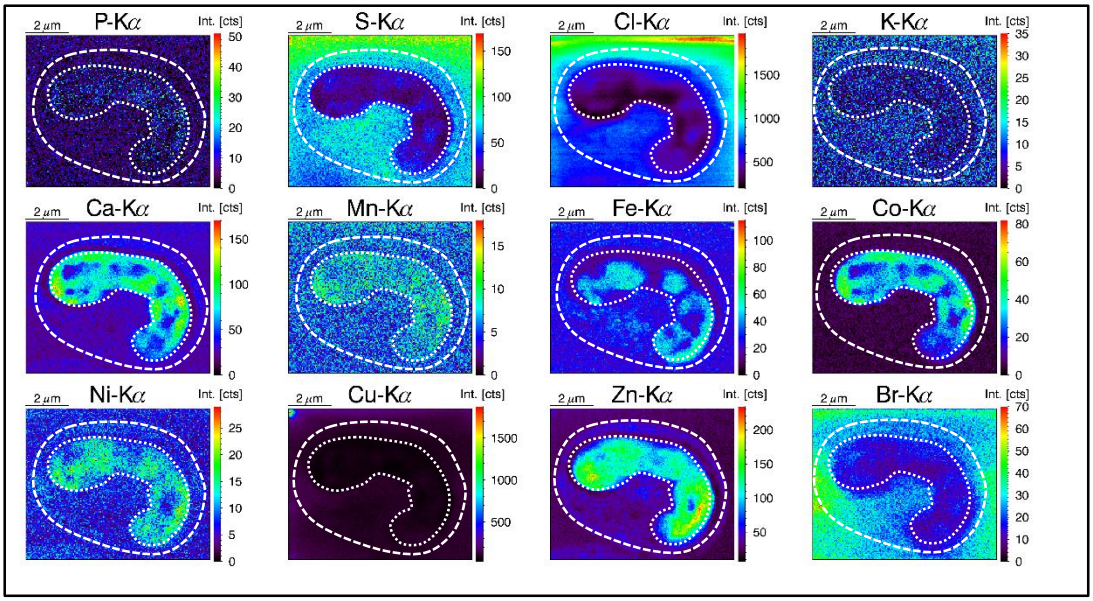

c)

NANO-XRF (CRYO)

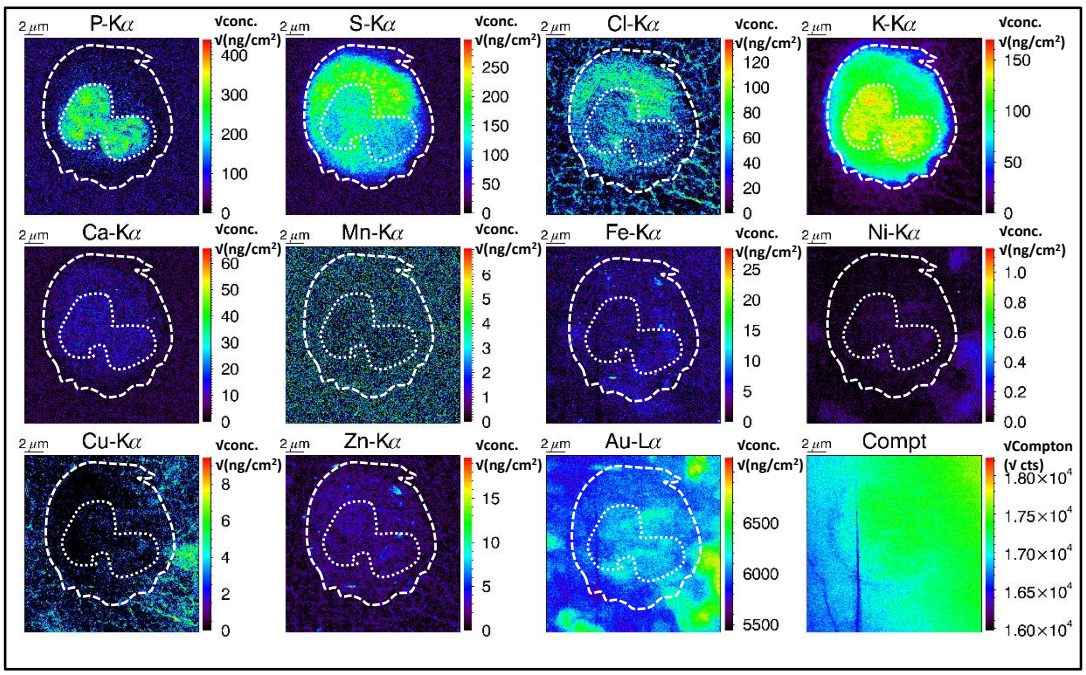

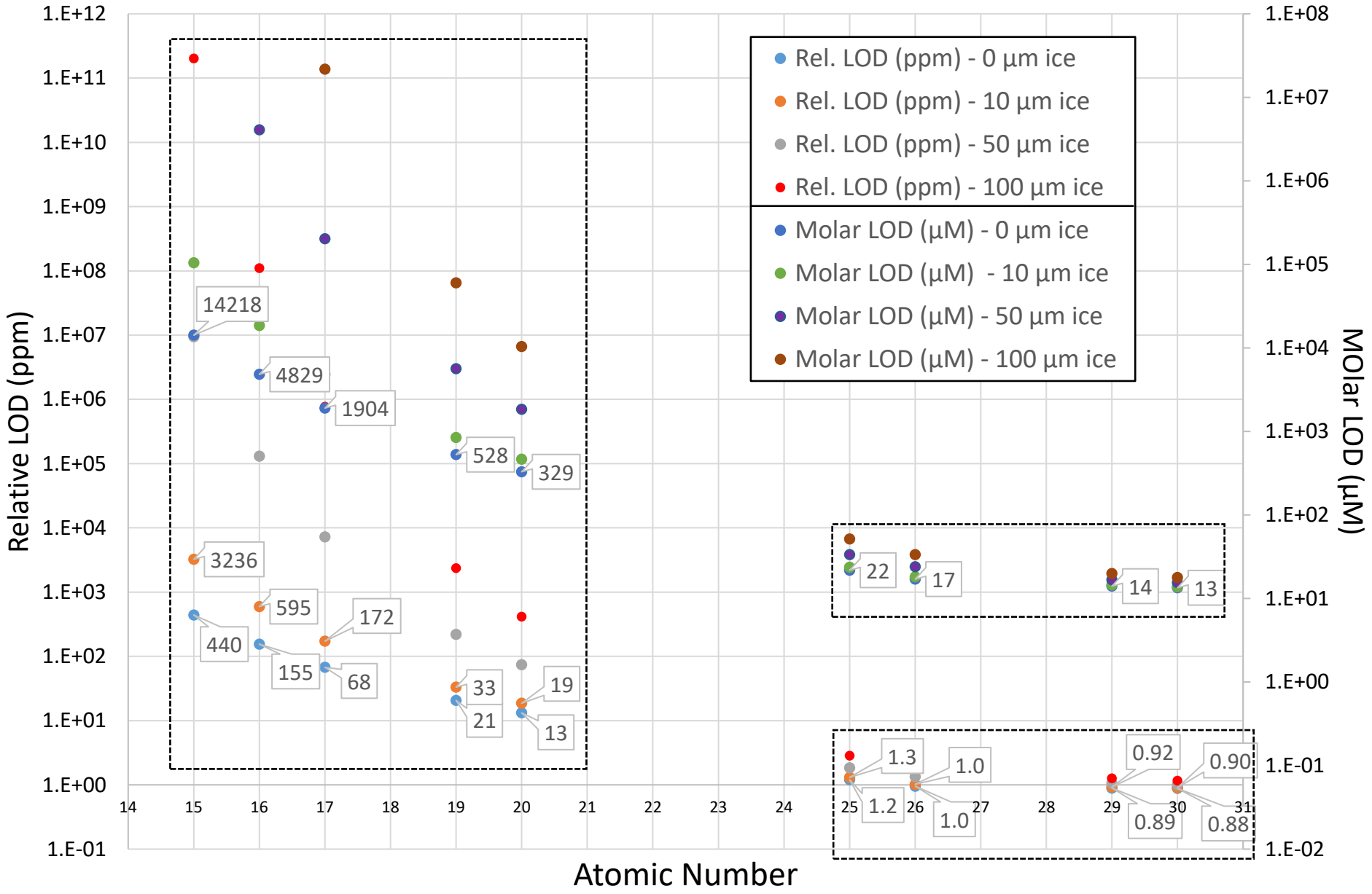
Rel. LOD (ppm) - 0 µm ice
Rel. LOD (ppm) - 10 µm ice
Rel. LOD (ppm) - 50 µm ice
Rel. LOD (ppm) - 100 µm ice
Molar LOD (µM) - 0 µm ice
Molar LOD (µM) - 10 µm ice
Molar LOD (µM) - 50 µm ice
Molar LOD (µM) - 100 µm ice
Relative LOD (ppm)
MOlar LOD (µM)
Atomic Number
1.E+12
1.E+11
1.E+10
1.E+09
1.E+08
1.E+07
1.E+06
1.E+05
1.E+04
1.E+03
1.E+02
1.E+01
1.E+00
1.E-01
1.E+08
1.E+07
1.E+06
1.E+05
1.E+04
1.E+03
1.E+02
1.E+01
1.E+00
1.E-01
1.E-02
14
15
16
17
18
19
20
21
22
23
24
25
26
27
28
29
30
31
14218
4829
1904
528
329
3236
595
172
440
155
68
33
19
21
13
22
17
14
13
1.3
1.0
1.2
1.0
0.92
0.90
0.89
0.88